Int J Fract
DOI 10.1007/s10704-013-9824-5

ORIGINAL PAPER

Crack patterns obtained by unidirectional drying of a colloidal suspension in a capillary tube: experiments and numerical simulations using a two-dimensional variational approach

C. Maurini · B. Bourdin · G. Gauthier · V. Lazarus

Received: 7 August 2012 / Accepted: 16 February 2013

Abstract Basalt columns, septarias, and mud cracks possess beautiful and intriguing crack patterns that are hard to predict because of the presence of cracks intersections and branches. The variational approach to brittle fracture provides a mathematically sound model based on minimization of the sum of bulk and fracture energies. It does not require any *a priori* assumption on fracture patterns and can therefore deal naturally with complex geometries. Here, we consider shrinkage cracks obtained during unidirectional drying of a colloidal suspension confined in a capillary tube. We focus on a portion of the tube where the cross-sectional shape cracks does not change as they propagate. We apply the variational approach to fracture to a tube cross-section and look for two-dimensional crack configurations minimizing the energy for a given loading level. We achieve qualitative and quantitative agreement between experiments and numerical simulations using a regularized energy (without any assumption on the cracks shape) or solutions obtained with traditional techniques (fixing the overall crack shape a priori). The results prove the efficiency of the variational approach when dealing with crack intersections and its ability to predict complex crack morphologies without any a priori assumption on their shape.

Keywords Brittle fracture mechanics · Griffith's fracture energy · Variational approach to fracture · Free-discontinuity problems · Drying of a colloidal suspension · Shrinkage cracks

C. Maurini
UPMC Univ Paris 6, UMR 7190, Institut Jean Le Rond d'Alembert, Boite courrier 161-2, 4 Place Jussieu, 75005 Paris, France
e-mail: corrado.maurini@upmc.fr

C. Maurini
CNRS, UMR 7190, Institut Jean Le Rond d'Alembert, Boite courrier 161-2, 4 Place Jussieu, 75005 Paris, France

B. Bourdin
Department of Mathematics and Center for Computation and Technology, Louisiana State University, Baton Rouge, LA 70803, USA
e-mail: bourdin@lsu.edu

G. Gauthier · V. Lazarus (✉)
UPMC Univ Paris 6, UMR 7608, FAST, Bat 502, Campus Univ, 91405 Orsay, France
e-mail: veronique.lazarus@upmc.fr

G. Gauthier · V. Lazarus
Univ Paris-Sud, UMR 7608, FAST, Bat 502, Campus Univ, 91405 Orsay, France
e-mail: gauthier@fast.u-psud.fr

G. Gauthier · V. Lazarus
CNRS, UMR 7608, FAST, Bat 502, Campus Univ, 91405 Orsay, France

1 Introduction

Complex fracture networks involving crack interactions and intersections are observed in a wide variety of situations associated with shrinkage loadings. Giant's Causeway (DeGraff and Aydin 1987), Port Arthur

Published online: 05 March 2013

tessellated pavement (Branagan and Cairns 1993), Bimini Road (Shinn 2009), Mars polygons (Mangold 2005), septarias (Seilacher 2001), fracture networks in permafrost (Plug and Werner 2001), and mud-cracks in coatings or paintings (Colina and Roux 2000) are a few examples that have intrigued people throughout history. Significant efforts have been devoted to reproducing similar phenomena in controlled experiments using either shrinkage induced by cooling (Yuse and Sano 1993; Ronsin et al. 1995; Yang and Ravi-Chandar 2001; Muller 1998), or drying (Hofmann et al. 2006; Goehring et al. 2006; Toramaru and Matsumoto 2004; Gauthier et al. 2010; Lazarus and Pauchard 2011). A large body of theoretical and numerical work has also be devoted to the propagation of preexisting cracks using classical tools of linear fracture mechanics (see for instance Bažant et al. 1979; Nemat-Nasser et al. 1980; Adda-Bedia and Pomeau 1995; Hofmann et al. 2006; Jenkins 2009; Bahr et al. 2010) or phase-field approaches (Corson et al. 2009). Despite all this work, many features of the complex crack networks observed in experiments are still poorly understood. In particular, a common limitation of all the references above is their inability to deal with cracks branching or intersecting (see Saliba and Jagla (2003) or Bahr et al. (2009) for some attempts at dealing with these issues.)

In contrast, the variational approach to fracture mechanics proposed by Francfort and Marigo (1998) provides a solution to these issues by treating the crack shape as a genuine unknown. In the context of brittle fracture, it can be seen as a natural extension of Griffith's energetic formulation Griffith (1920). It is based on the minimization amongst all admissible crack sets and possibly discontinuous displacement fields of a total energy functional consisting of the sum of a bulk (elastic) and a surface term proportional to the surface of the cracks (or their length in two dimensions). The minimization problem is challenging because it is in general technically not possible to test all crack configurations. Instead, a regularized energy is used to the numerical prediction of complex crack patterns without any preliminary assumption on the overall cracks shape. In recent years, efforts have mainly focused on its theoretical and numerical developments (Bourdin et al. 2000, 2008) . However, applications to the prediction of complex crack patterns with a close qualitative but also quantitative comparison to experimental results are still lacking, in particular when crack intersections are involved. This paper constitute a first effort aiming at filling this gap. We apply the variational approach to the controlled drying of a colloidal suspension in a capillary tube for which fascinating experimental results have been obtained when the colloidal suspension gradually turns into a drained porous solid matrix.

During drying. the natural shrinkage of the solid matrix which is prevented by the strong adhesion to the wall of the tube, gives rise to high tensile stresses and to a large number of disordered cracks which gradually self-organize and propagate with a constant cross-sectional geometry. The cross-sectional shape depends on the geometry of the tube and the drying conditions (e.g. Allain and Limat 1995; Dufresne et al. 2003, 2006; Gauthier et al. 2007) and looks mostly like stars where several straight cracks intersect at or near a single point. In this paper, we focus on the two-dimensional problem of the prediction of these cross-sectional crack shapes, but we refrain to solve the entire, far more complex, three-dimensional propagation problem.

Recently, Gauthier et al. (2010) modeled the drying porous solid by an elastic material loaded by a tensile prestress and showed that the observed cross-sectional crack patterns can be correctly predicted by energy minimization amongst a given family of cracks, namely arrays of parallel cracks for flat tubes or star-shaped cracks for cylindrical ones. This demonstrated that their simple model captures the key physical ingredients. However, in this first study the overall crack shape was fixed a priori. Here, we extent the experiments of Gauthier et al. (2010) to non axisymmetric square geometry, for which the crack shape is more difficult to guess, and revisit them through the variational method developed by Bourdin et al. (2000) using the physical model demonstrated previously. We show that this method provides a qualitative and quantitative description of the different cross-sectional crack patterns observed experimentally without any preliminary shape assumptions.

The outline of the article is the following. The experimental setup is described in details in Section 2, illustrating the results obtained by changing the suspension and the drying velocities. In addition to the experiments on circular tubes previous reported in Gauthier et al. (2010), new experiments on capillary tubes with square cross-section highlight the relation between the tube cross-sectional shape and the crack pattern. In Sect. 3, we focus on the regime where the cross-sectional geometry of the crack does not evolve. We describe our

two-dimensional model assuming a linear elastic brittle solid under plane-strain conditions and a drying loading introduced through a tensile isotropic inelastic strain. In Sect. 4, we recall the results of Gauthier et al. (2010) and search for least-energy solutions amongst the class of star-shaped cracks. This allows us to identify some semi-analytical solutions to be used as reference for the verification of the numerical implementation. We then seek to fully identify the crack geometry by numerical minimization of a regularized form of the total energy functional (Sect. 5). There, we briefly describe the details of the approach then introduce a selection principle. We illustrate our approach by providing a qualitative and quantitative comparison with experimental and semi-analytical results in Sect. 7.

2 Experiments

Experiments are conducted in circular or square glass capillary tubes. The height of the tubes is typically 10 cm and the radius of the cross-section of the circular tubes are $R = 0.05$ mm, $R = 0.15$ mm, $R = 0.5$ mm or $R = 0.75$ mm while the edge length of the square tubes is $2R = 1$ mm. According to the manufacturer, the precision on the radii is 10 %. The tubes are positioned in vertical orientation and colloidal suspension is sucked up from their bottom until they are 3/4 full (see Fig. 1a). The top of the tubes is closed and maintained at a pressure slightly below that of the surrounding. Because of the capillary effect, this prevents the fluid from flowing under gravity. Two type of colloids have been used, both made of water silica dispersions: Ludox™HS40 and SM30 designated as HS40 and SM30 in the following. HS40 and SM30 differ in mass fraction (30 and 40 % mass fraction of silica particles for SM30 and HS40 respectively) and in particle size ($r \simeq 3.5$ nm and $r \simeq 6$ nm for SM30 and HS40 respectively). As soon as capillary tubes are filled, water contained in the suspension evaporates from the bottom of the tube. In the early stages of drying, particles aggregate at the wall close to the open edge until they fill a section of the tube. Once this porous layer is formed, the liquid interface is composed of a high number of meniscus with a typical radius of curvature of the order of the particle size. These meniscus generate high negative pressure that cause the water to flow. The water flow drives the silica particles to accumulate at the porous upper surface and a porous plug further develops. Drying is then governed by Darcy's law (Dufresne et al. 2003, 2006). Since the pressure gradient decreases as the plug extends, drying velocity decreases. However for plugs long enough (∼20 tube diameters) drying velocity is almost constant over few diameters (∼5). It is this region that is studied in the sequel. Once the plug height is about twenty times the diameter, the tubes are placed in controlled environment maintained at a constant relative humidity (RH) and temperature (T). Experiments are performed at three different conditions: (i) at a room temperature $T \simeq 20\,°C$ and RH maintained below 10% by using desiccant, (ii) at $T \simeq 20\,°C$ and RH maintained over 90 % by introducing water in the chamber, (iii) at $T \simeq 3\,°C$ and RH $< 10\,\%$.

The high negative capillary pressure, imposed by the interface, in the draining fluid generates high tensile stresses in the gel (Dufresne et al. 2003) that cause it to crack. The cracks pattern can be visualized either by transparency, which allows to follow the crack propagation during the drying, or by cutting the tube at the desired height, to observe the cross-sectional crack shape. Disordered cracks are first observed in the bottom. As the plug extends, the cracks self-organize, become vertical and grow along the drying direction preserving their cross-sectional shape for a length corresponding to several tube diameters (Gauthier et al. (2007) for a more detail description of the evolution). Examples are given in Fig. 1b. For square tubes, two perpendicular diagonal cracks appear. For circular tubes, star-shaped cracks where the tube cross section is divided into n sectors (with a central angle $2\pi/n$) are observed. Once these cracks have appeared, the porous medium continues to dry and to undergo high tensile stresses leading to secondary cracks appearing later on along the cross section of the tube.

In the sequel, we focus only on (i) the tube region where the crack cross-sectional geometry is independent of the depth and on (ii) the time period after the disordered cracks have self-organized and before the appearance of secondary cracks. We observe that the cross-sectional crack shape for a given suspension and tube geometry depends on the drying conditions through the drying velocity only. Indeed drying at $T \simeq 3\,°C/RH \leq 10\,\%$ or at $T \simeq 20\,°C/RH \geq 90\,\%$ gives the same crack tip velocities and the same crack patterns. Thus we refer to experiments conducted at $T \simeq 3\,°C/RH \leq 10\,\%$ or at $T \simeq 20\,°C/RH \geq 90\,\%$ as slow velocity (SV) experiments, and those conducted at $T \simeq 20\,°C/RH \leq 10\,\%$ as high velocity (HV)

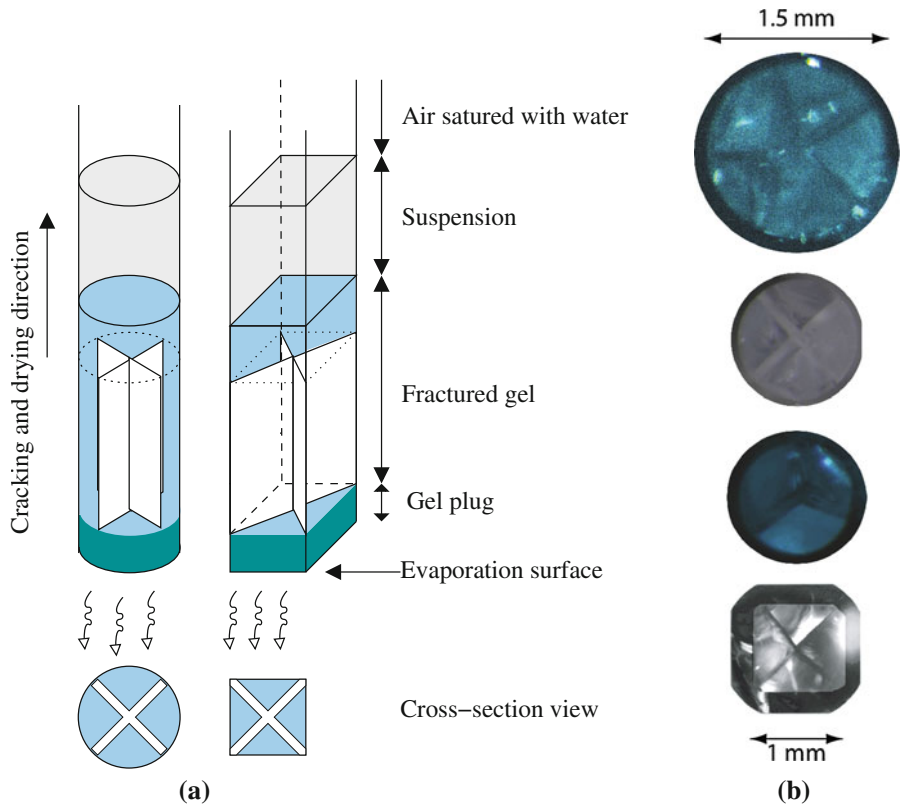

Fig. 1 A glass capillary tube oriented vertically is filled with a colloidal suspension; the *opened bottom* edge allows for evaporation of the water in an environment maintained at a constant relative humidity (RH) and temperature (T). The cross-sectional shape of the cracks depend on the tube shape and size and on the drying conditions. **a** Experimental setup and sketch of the self-organized star-shaped cracks. **b** Pictures of some cross section cuts (the colors depend on the light used)

experiments. A summary of experiments made can be found in Table 3 (Sect. 7). For small enough diameters, the number of cracks observed increases with the diameter. For larger containers, it is obvious that the crack pattern in the center becomes independent of the walls of the tube. We also observe that changing the drying conditions from SV to HV or HV to SV during the same experiment produces a transition between the two cross-sectional crack patterns obtained in pure HV and SV experiments (Gauthier et al. 2010) and that this rearrangement takes places over a distance approximately equal to the tube diameter. This suggests that history effects can be neglected.

3 Model

3.1 Basic hypotheses

In this work, we focus our attention on the steady-state regime where the cross-sectional geometry of the cracks remains constant. We model the problem as a two-dimensional plane-strain one on the cross-section of the tube. We assume that (i) the only effect of drying is to introduce an inelastic strain $\boldsymbol{\epsilon}_0 = \epsilon_0 \mathbf{1}$, where $\mathbf{1}$ denotes the identity matrix and $\epsilon_0 < 0$ is assumed constant throughout the cross section of the domain and that (ii) the solid adheres perfectly to the tube walls. Following the variational approach to brittle fracture (Francfort and Marigo 1998), for a given loading ϵ_0, we search for the deformation and crack configuration corresponding to a minimum of the total energy defined as the sum of the bulk elastic energy and the crack surface energy. The latter is of Griffith type, that is: the energy $\mathcal{S}(\gamma)$ per height unit, associated to a crack set γ is proportional to its length and given by

$$\mathcal{S}(\gamma) := G_c \mathcal{L}(\gamma),$$

where G_c is the specific fracture energy of the material, and $\mathcal{L}$ denotes the length of the crack. For the elastic energy, we suppose that the material is perfectly elastic prior to failure, and we adopt the linearized theory under the small displacement approximation. Finally, we assume that the crack surfaces are stress-free.

In the above formulation of the fracture mechanics problem, we simply look for the optimal cross-sectional crack pattern, according the energy minimality criterion, for given values of the loading ϵ_0. We do not introduce any concept of history dependence of the crack patterns. We solve a two-dimensional *static* problem and not the three-dimensional *quasi-static* evolution problem, in which one looks for the initiation and propagation of cracks as a function of time starting from a well-defined initial condition. Omitting history effects is suggested by the reversibility of the cross-sectional experimental patterns, using a two-dimensional approximation by the experimental observations of depth-independence of the cross-sectional crack patterns. The good agreement between numerical and experimental findings presented in Sect. 7 also justifies this hypothesis, *a posteriori*.

3.2 Variational fracture model

Let us introduce the following equivalent two-dimensional inelastic strain defined by $\boldsymbol{\epsilon}_0^{2d} = (1+\nu)\epsilon_0\,\mathbf{1}_2$, where $\mathbf{1}_2$ is the 2×2 identity matrix. With this notation and the aforementioned hypotheses, the strain energy can be written as:

$$w(\boldsymbol{\epsilon},\boldsymbol{\epsilon}_0) := \frac{E}{2(1+\nu)}\left(\frac{\nu}{(1-2\nu)}\mathrm{tr}^2(\boldsymbol{\epsilon}-\boldsymbol{\epsilon}_0^{2d}) + (\boldsymbol{\epsilon}-\boldsymbol{\epsilon}_0^{2d})\cdot(\boldsymbol{\epsilon}-\boldsymbol{\epsilon}_0^{2d})\right) \tag{1}$$

where E and ν are the Young modulus and the Poisson ratio of the material, $\boldsymbol{\epsilon}$ is the symmetric second-order 2×2 matrix representing the linearized plane strain, tr denote the trace operator, and the dot is used for the scalar product. In linear elasticity, kinematic compatibility implies that $\boldsymbol{\epsilon}(u) = \frac{1}{2}(\nabla u + \nabla u^T)$, where u is the displacement field, ∇ the gradient operator, and the superscript T denotes the transpose operator. We parameterize the inelastic strain $\boldsymbol{\epsilon}_0^{2d}$ representing the drying loading by a non dimensional drying intensity $\bar{\epsilon}$, defined by (see the first remark at the end of this section)

$$\boldsymbol{\epsilon}_0^{2d} := -\bar{\epsilon}\sqrt{\frac{G_c}{ER}}\,\mathbf{1}_2 \tag{2}$$

where R is a characteristic length associated with the cross-section, typically its radius. Hence, the potential energy $\mathcal{P}_{\bar{\epsilon}}$ of the cross-section occupying the open set $\mathcal{C}$ and associated to a displacement field u and a crack set γ for a loading parameter $\bar{\epsilon}$ is given by

$$\mathcal{P}_{\bar{\epsilon}}(u,\gamma) := \int_{\mathcal{C}/\gamma} w_{\bar{\epsilon}}(\boldsymbol{\epsilon}(u))\mathrm{d}S, \quad \text{with}$$
$$w_{\bar{\epsilon}}(\boldsymbol{\epsilon}) := w\left(\boldsymbol{\epsilon}, -\bar{\epsilon}\sqrt{G_c/ER}\,\mathbf{1}_2\right). \tag{3}$$

The total energy is defined as the sum of the potential energy and the surface energy required to create the cracks:

$$\mathcal{E}_{\bar{\epsilon}}(u,\gamma) := \mathcal{P}_{\bar{\epsilon}}(u,\gamma) + \mathcal{S}(\gamma). \tag{4}$$

For any given loading parameter $\bar{\epsilon}$, we seek to find the crack set γ and displacement field u as the global minimizer of (4) amongst *any* admissible crack set and kinematically admissible displacement fields. The admissible crack sets consist of all possible curves or sets of curves inside the boundary of $\mathcal{C}$. For any given crack set γ, the space of the admissible displacements is

$$\mathcal{U}(\gamma) := \{u \in H^1(\mathcal{C}\setminus\gamma;\mathbb{R}^2), \quad u = 0 \text{ on } \partial\mathcal{C}\}, \tag{5}$$

i.e. it consists of all vector valued fields satisfying the adhesion boundary condition and sufficiently smooth (square integrable with square integrable first derivatives) on the uncracked domain. More precisely, the global minimality condition can be expressed as:

$$\text{Find } \gamma\subset\mathcal{C},\ u\in\mathcal{U}(\gamma): \quad \mathcal{E}_{\bar{\epsilon}}(u,\gamma) \le \mathcal{E}_{\bar{\epsilon}}(u^*,\gamma^*), \quad \forall\gamma^*\subset\mathcal{C},\ u^*\in\mathcal{U}(\gamma^*). \tag{6}$$

Remark 1 The scaling factor $\sqrt{G_c/ER}$ in (2) renders all the results, presented in terms of $\bar{\epsilon}$ in the rest of the paper, independent of the material constants and cross-sectional dimension. Other choices for the relevant non dimensional parameter are possible. In particular, as in Gauthier et al. (2010), one could also chose to parameterize the loading in terms of the Griffith length $L_c := EG_c/\sigma_0^2$, where σ_0 is a prestress. After some calculations, one can relate $\bar{\epsilon}$ and L_c by

$$L_c = \frac{R}{\bar{\epsilon}^2}(1-2\nu)^2(1+\nu)^2. \tag{7}$$

This relation will be useful in Sect. 7 as it will allow us to estimate the value of $\bar{\epsilon}$ for various experiments.

4 Simple illustration: star-shaped cracks in circular tubes

Before we dwell upon numerical implementation and numerical experiments, it is possible to gain some

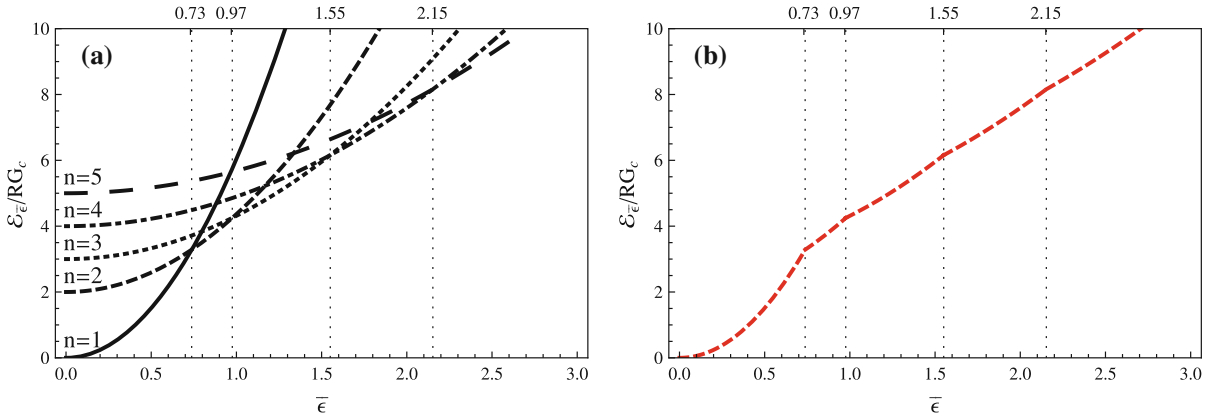

Fig. 2 Energy minimization amongst star-shaped cracks. **a** Total energy associated with γ_n for $n = 1, 2, 3, 4, 5$. **b** The *lower* envelope of the family of *energy curves* gives the energy of the minimizer

valuable insight on the model by restricting the set of admissible cracks to radial ones. It is essentially equivalent to the work of Gauthier et al. (2010) with the difference that the loading parameter we consider here is the inelastic strain instead of the prestress. The construction of the semi-analytic radial crack solution will also be used as a reference point for the analysis of the numerical solutions and the *verification* of the suggested numerical approach.

We consider a circular tube with radius R and star-shaped cracks. By γ_n, $(n > 1)$, we denote a curve consisting of the union of n equi-distributed radial segments partitioning the tube into n polar regions. By analogy, we write $\gamma_1 = \emptyset$. Our motivation for considering such geometries comes from the fact that they are frequently observed in the experiments, at least for small values of n.

Note first that for a given crack pattern γ, the potential energy can be computed by solving a linear elasticity problem, and we write

$$\mathcal{P}_{\bar\epsilon}(\gamma) := \min_{u\in\mathcal{U}(\gamma)} \mathcal{P}_{\bar\epsilon}(u,\gamma), \tag{8}$$

the potential energy of the equilibrium displacement. It is then easy to see that the form of the strain energy density (1) implies that $\mathcal{P}_{\bar\epsilon}(\gamma) = \bar\epsilon^2\mathcal{P}_1(\gamma)$, so that we can rewrite the total energy in the form

$$\mathcal{E}_{\bar\epsilon}(\gamma) = \bar\epsilon^2\mathcal{P}_1(\gamma) + \mathcal{S}(\gamma). \tag{9}$$

Furthermore, for a star-shaped crack γ_n, using eq. (1), one has

$$\mathcal{E}_{\bar\epsilon}(\gamma_n) = \bar\epsilon^2\mathcal{P}_1(\gamma_n) + n\,G_c R. \tag{10}$$

For $n = 1$ the problem can be solved in closed form, the elastic equilibrium is achieved for $u = 0$ and the total energy is $\mathcal{E}_{\bar\epsilon}(\emptyset) = \mathcal{P}_{\bar\epsilon}(\emptyset) = \bar\epsilon^2\pi G_c R/(1+\nu)(1-2\nu)$. For $n > 1$, $\mathcal{P}_1(\gamma_n)$ can be computed by a simple finite element computation. In this setting, for a given loading parameter $\bar\epsilon$, energy minimization reduces to a discrete minimization problem with respect to n. And the total energy of the solution as a function of the loading parameter can be obtained by taking the lower envelope of the family of energy curves associated to each configuration.

Figure 2a represents the total energy associated with γ_n as a function of the loading parameter $\bar\epsilon$ for $n = 1, 2, 3, 4, 5$ and $\nu = 0.3$. Using this graph and the global minimality principle (6), it is easy to identify the optimal crack configuration associated with a given load (the branch of the energy with the smallest value for a given $\bar\epsilon$) as well as the bifurcation points upon which the geometry of the optimal crack set changes (the crossing points upon which the energy branch achieving minimality changes). We obtain that there exists a family $(0 = \bar\epsilon_0, \bar\epsilon_1, \bar\epsilon_2, \dots)$ of critical loadings such that for $\bar\epsilon_{i-1} < \bar\epsilon < \bar\epsilon_i$, $i = 1, 2, \dots$, the optimal crack configuration is *any* curve in the family γ_i. Of course, in the absence of defects or impurities, the solution for a given loading parameter is unique up to a rotation. The numerical values of the critical loadings are $\bar\epsilon_1 \simeq 0.73$, $\bar\epsilon_2 \simeq 0.97$, $\bar\epsilon_3 \simeq 1.55$, $\bar\epsilon_4 \simeq 2.15$, and $\bar\epsilon_5 \simeq 2.76$. Figure 2b shows the energy associated with the optimal configuration, obtained by taking the lower envelope of the family of curves plotted in the left.

Before closing this simple example, we stress again that this analysis is based upon the assumption that the optimal crack geometry is a star-shaped pattern. As we will see in the following sections, relaxing this hypothesis allows to show that the star-shape cracks are indeed optimum for not too high loading and can yield to more complicated but energetically least costly crack patterns for higher loading.

5 General case: minimization over arbitrary crack geometries

In the variational formulation (6), the admissible displacement fields are potentially discontinuous across cracks γ, but the location of the potential discontinuities themselves is not known a priori. This renders the numerical minimization of (4) challenging as most numerical methods such as cohesive, discontinuous or extended finite element methods require at least *some* a priori knowledge of the crack path or of its topology. Indeed, this problem falls into the broader class of *free discontinuity problems* for which a wealth of mathematical and numerical literature now exists (Ambrosio et al. 2000). In the following, we solely focus on the numerical implementation using an extension of that proposed in Bourdin et al. (2000) and Bourdin (2007). It relies on the concept of variational approximation of the total energy functional by a family of regularized elliptic functionals (Ambrosio and Tortorelli 1990, 1992; Braides 1998), depending on a scalar regularization parameter ℓ, and discretized by standard finite elements. In the regularized functional, sharp cracks are represented by a smooth auxiliary variable α in the sense that for small ℓ, the non-zero values of α are localized along thin bands of high strains which can be interpreted as smeared representation of the cracks. From a technical standpoint, the approximation takes place in the sense of Γ-convergence (Braides 2002), i.e. one can prove that as the regularization parameter ℓ goes to 0, the global minimizers and the energy values of the regularized functionals approaches those of the total energy with sharp discontinuities. We briefly recall the numerical approach below and refer the reader to the literature for further details. Note however that all the previous studies on the numerical simulations on fracture mechanics using the variational approach focussed on the *quasi-static* evolution problem. The fact that we consider here the *static* problem entails further issues on the selection of the solutions.

5.1 Regularization by elliptic functionals

The main idea of our approach was originally developed by Ambrosio and Tortorelli (1990, 1992) for an image segmentation (Mumford and Shah 1989) problem, and adapted to fracture mechanics by Bourdin et al. (2000). One introduces a small parameter ℓ with dimension of a length, a secondary variable α taking its values in $[0, 1]$ and representing the crack set, and the regularized functional

$$\mathcal{E}_{\bar{\epsilon}}^{(\ell)}(u,\alpha) := \int_{\mathcal{C}} ((1-\alpha)^2 + k_\ell) w_{\bar{\epsilon}}(\boldsymbol{\epsilon}(u)) \mathrm{d}S + \frac{3G_c}{8} \int_{\mathcal{C}} \left[\frac{\alpha}{\ell} + \ell \, \nabla\alpha \cdot \nabla\alpha \right] \mathrm{d}S. \quad (11)$$

Hence, one approximates the solution of (6) by those of the following minimization problem:

$$\min_{u \in \mathcal{U}, \alpha \in \mathcal{A}} \mathcal{E}_{\bar{\epsilon}}^{(\ell)}(u,\alpha) \quad (12)$$

where $\mathcal{U} = \{u \in H^1(\mathcal{C};\mathbb{R}^2),\ u = 0 \text{ on } \partial\mathcal{C}\}$ and $\mathcal{A} = \{0 \le \alpha \le 1,\ \alpha \in H^1(\mathcal{C};\mathbb{R}),\ \alpha = 0 \text{ on } \partial\mathcal{C}\}$. The main advantages of this regularized formulation is that it eliminates the issue of representing discontinuous fields when their discontinuity set is not known *a priori*. It also reduces energy minimization with respect to any admissible crack geometry to minimization with respect to a smooth field, a much simpler problem. In addition, it can be discretized numerically using standard continuous finite elements.

This regularized functional can be shown to converge in the sense of Γ-convergence to the total energy (4). This implies that for any $\bar{\epsilon}$, the global minimizers of $\mathcal{E}_{\bar{\epsilon}}^{(\ell)}$ converge as $\ell \to 0$ to global minimizers of $\mathcal{E}_{\bar{\epsilon}}$, and that each term in (11) converges to the matching one in (4). The parameter k_ℓ is a small residual stiffness introduced mainly for numerical purposes which is known to have very little impact on the minimizers. The convergence result is valid provided that $k_\ell = o(\ell)$. We refer the interested reader to Braides (2002), Dal Maso (1993) for more details on Γ–convergence and to Braides (1998); Bourdin et al. (2008) for details on the approximation of $\mathcal{E}_{\bar{\epsilon}}$ by $\mathcal{E}_{\bar{\epsilon}}^{(\ell)}$. Formally, as ℓ goes to 0, α remains close to 0 away from the cracks, and approaches 1 along the cracks.

For small but non-zero values of ℓ, both arguments u and α of $\mathcal{E}_{\bar{\epsilon}}^{(\ell)}$ are continuous functions with high gradients (of order $1/\ell$) in bands of width ℓ. The regularized energy we use here is slightly different from the one in Bourdin et al. (2000) and Bourdin et al. (2008). The form used here has some advantages from numerical and theoretical standpoints, which are not discussed here. The interested reader is referred to Pham et al. (2011a) for further details on this point.

Several authors noticed that the regularized form of the energy may be interesting as a model *per se* (Del Piero et al. 2007; Amor et al. 2009; Lancioni and Royer-Carfagni 2009; Freddi and Royer-Carfagni 2010). In particular, it may be interpreted as the energy of a gradient damage model, where α plays the role of the damage field and ℓ of the internal length (Pham et al. 2011a,b). The regularized formulation also resembles phase field approximations of sharp interfaces models (Hakim and Karma 2009; Corson et al. 2009). However, there are significant differences between our numerical approach and the phase-field fracture models. Even in the static or quasi-static case, phase-field models are formulated as a rate-dependent evolution equation and stated as fracture models *per se*.

In the present work, we do not see the regularized formulation as a model in itself, but we consider it as a mere numerical approximation of the total energy of the variational approach of Francfort and Marigo (1998). This approximation is deeply rooted in the mathematical literature on free-discontinuity problems (Braides 1998). In particular the minimization principle for the regularized energy is derived from that of the variational model in the *static* case, which explains our focus on *global* minimizations even though for gradient damage laws, there are *quasi-static* models based on local minimality. This comes with an added difficulty, that of finding *global* minimizers of a non-convex functional. This is a very challenging issue that we do not claim to fully address in this article. Instead, we propose some strategies leading to *local* minima with decreasing energy which are therefore better candidates for *global* optimality.

5.2 Numerical implementation

The numerical minimization of (11) is implemented in a way similar to that described in Bourdin (2007). We discretize the regularized energy by means of linear Lagrange finite elements over an unstructured mesh. As long as the mesh size h is such that $h = o(\ell)$, the Γ-convergence property of (11) to (4) is also true for the discretization of the regularized energy (see Bellettini and Coscia (1994); Bourdin (1999); Burke et al. (2010) for instance). This compatibility condition leads to fine meshes, which are better dealt with using parallel supercomputers. We use PETSc (Balay et al. 1997, 2010, 2011) for data distribution, parallel linear algebra, and TAO (Benson et al. 2010) for the constrained optimization. In order to avoid preferred directions in the mesh, we use the Delaunay-Voronoi mesh algorithm implemented in Cubit, from Sandia National Laboratories (see Negri (1999); Chambolle (1999) for an analysis of the anisotropy induced by structured meshes or grids).

Due to the size of the problems, *global* minimization algorithms are not practical. Instead, we look for local minima by imposing numerically the first-order necessary optimality conditions for (12). We notice that although (11) is not convex, it is convex with respect to each variable individually. We alternate minimizations with respect to u and α, an algorithm akin to a block Newton method or a segregated solver. Note that minimization with respect to u is equivalent to solving a simple linear elasticity problem, but that minimization with respect to $\alpha \in [0, 1]$ requires an actual box-constrained minimization algorithm. Of course, as the total energy is not convex, one cannot expect convergence to a *global* minimizer. However, one can prove that the alternate minimization process is unconditionally stable and globally decreasing and that it leads to a stationary point of (11) which may be a local (or global) minimizer or a saddle point of the energy.

This approach may fall short of our stated goal of achieving *global* minimization of the regularized energy as the outcome of a descent-based algorithms for such a non-convex problem may depend on the regularization parameter ℓ, the mesh size and type, and the starting guess. From a practical standpoint we observe that the algorithm is quite robust with respect to the mesh discretization, provided that the regularization length ℓ is large enough compared to the mesh size. However it can be sensitive with respect to the initial value of α. Different choices of the initial guess α or of the regularization parameter ℓ can lead to convergence to different solutions. This issue is much more troublesome in the present case, in which we attempt to solve

a *static* problem, than when considering a *quasi-static evolution*. In the quasi-static setting, one can follow the evolution of the crack state as the loading increases starting from a well-defined initial state, and formulations based on local minimality of (11) may gain a pertinent physical interpretation, linking the critical load for fracture initiation to the value of the regularization parameter (Pham et al. 2011a). In the present static settings, for the lack of the concepts of history and irreversibility, there is no physically consistent base state and a selection criterion of the solutions obtained by local minimization is necessary. Consistently with the Francfort-Marigo model, we adopt a least energy criterion: among a set of local minima corresponding to a given $\bar{\epsilon}$ and different choices of the initial guesses, we select the one with lowest energy. Again, we make no claim of achieving global minimization of the regularized energy. In our mind, that our numerical simulations match the semi-analytical solutions and the experiments is the best (although still somewhat unsatisfying) argument we can give in favor of this approach.

6 Numerical simulations

We first illustrate our numerical approach on circular tubes (Sect. 6.1). The comparisons of the numerical results with the semi-analytical results for the star-shaped cracks from Sect. 4 gives a partial *verification* of our numerical approach (Sect. 6.2). Results for square tubes are briefly presented in Sect. 6.3.

6.1 Crack shapes for circular tubes

The presentation is organized in three steps: (i) first we report the results obtained as a function of the drying intensity $\bar{\epsilon}$ and the non-dimensional the internal length $\bar{\ell} = \ell/R$, by taking the elastic solution as initial guess for the alternate minimization algorithm; (ii) then we show that a ℓ-refinement technique may reduce the dependence of the results on $\bar{\ell}$ and produce lowest energy solutions; (iii) finally, using the fact that the elastic energy is a 2-homogeneous function of $\bar{\epsilon}$, we identify for each value of the loading the crack shape with the lowest energy among all those obtained after ℓ-refinement.

6.1.1 *Results as function of $\bar{\epsilon}$ and $\bar{\ell}$ taking the elastic uncracked state as initial guess*

Figure 3 presents the field α obtained by numerical minimization of (11) for various choices of the parameters $\bar{\epsilon}$ and $\bar{\ell}$ with a tube of radius $R = 1$. The material parameters $(E,\ G_c)$ were set to 1 without loss of generality, and the Poisson ratio to 0.3. In each computation, the mesh size was $h = 0.025$ and the residual stiffness was set to $k_\ell = 10^{-6}$. The alternate minimization algorithm was initialized with $\alpha = 0$. The value 1 (corresponding to cracks) of α is encoded in red and the value 0 (the un-cracked material) in blue. A first glance at the table highlights the wide variety of crack geometries obtained, and that the complexity of the fracture pattern increases with the loading parameter. Again we stress that no hypothesis on this geometry is made in the model and that the shape of the crack patterns is purely an outcome of the minimization of the regularized energy. We observe that the width of the transition zone from 1 to 0 decreases as $\bar{\ell}$ goes to 0, which is consistent with the Γ-convergence property stated in Sect. 5. For "large" values of $\bar{\ell}$, when the width of the transition zone is of the order of the diameter of the tube and as $\bar{\epsilon}$ increases, one cannot distinguish between neighboring cracks (see for instance the case $\bar{\ell} = 0.2$ for $\bar{\epsilon} = 5.0$).

A closer look at Fig. 3a highlights the dependency of the crack pattern upon the regularization parameter $\bar{\ell}$. See for instance how for a loading parameter $\bar{\epsilon} = 1.2$, we obtain a triple junction for $\bar{\ell} = 0.2$, but a complex crack made of two triple junctions for $\bar{\ell} = 0.1$, and no cracks at all for $\bar{\ell} = 0.05$. Each of these configuration correspond to a critical point of the energy (11) (likely local minimizers). It may be theoretically shown that below a critical load $\bar{\epsilon}^*(\bar{\ell})$ depending on $\bar{\ell}$, the un-cracked configuration $\alpha = 0$ is a stable critical point of (11). In a simpler 1d setting, it is known that $\bar{\epsilon}^*(\bar{\ell}) = \mathcal{O}(1/\sqrt{\bar{\ell}})$ (Pham et al. 2011a). Here, we observe that $\bar{\epsilon}^*(\bar{\ell})$ increases as $\bar{\ell} \to 0$. When alternate minimizations iterates "escape" the un-cracked solution, they converge to the "nearest" critical point which may or may not be the *global* minimizer of the energy. If the regularized model (11) is seen as a gradient damage model with internal length $\bar{\ell}$ (see Pham et al. 2011a), and if one focusses on criticality instead of global minimality, this behavior is consistent with a *scale effect* linking the critical load and the ratio of the structural dimension and the internal length (Bažant 1999).

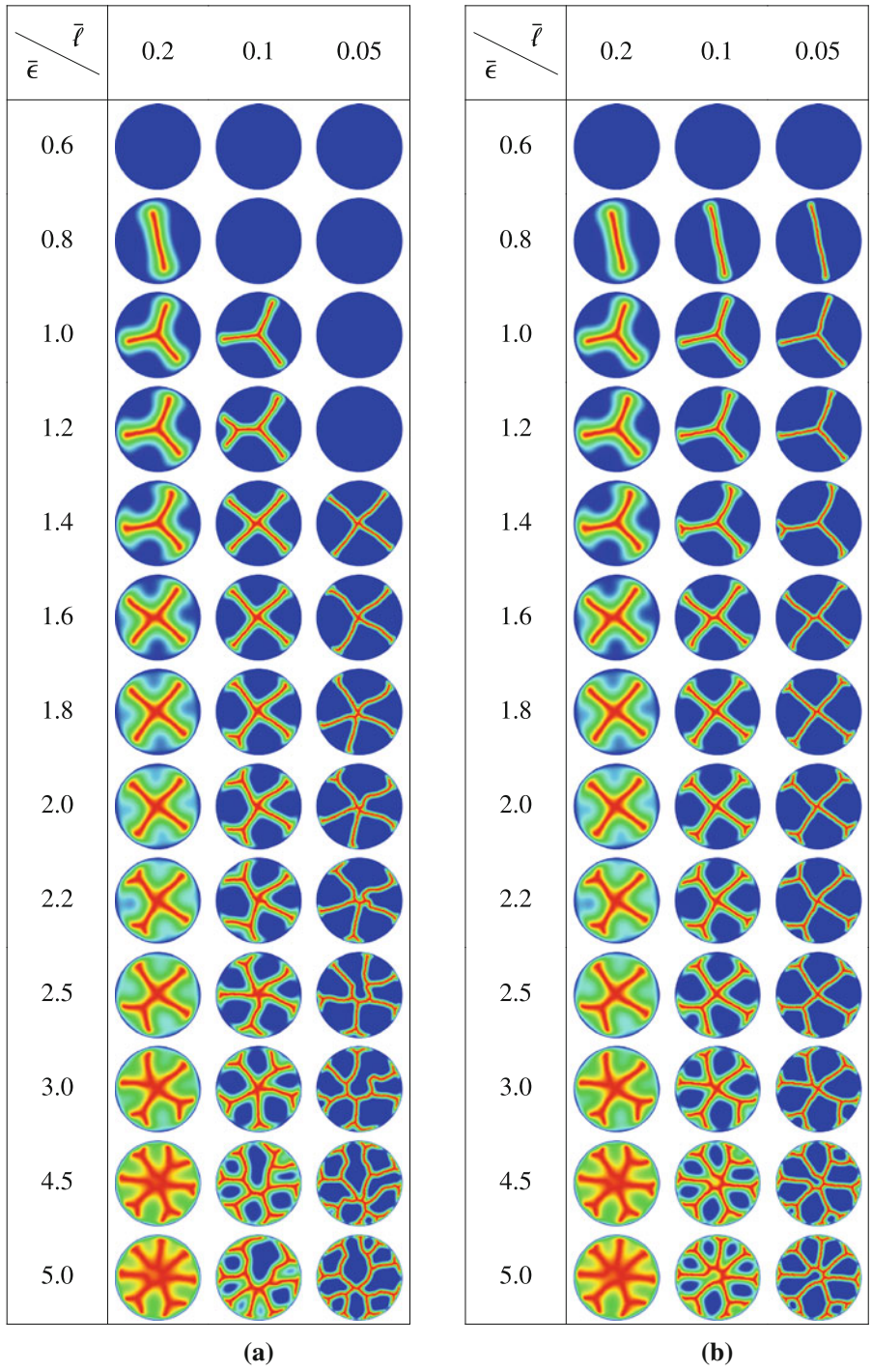

Fig. 3 Numerical results by minimization of functional (11) for circular cross-sections. The results are obtained using uniform Delaunay-Voronoi unstructured meshes with size $h = 0.025$ on disk of radius $R = 1$. The material properties are $E = 1,\ G_c = 1,\ \nu = 0.3$. **a** Direct numerical simulations. Each problem was solved independently initializing the alternate minimizations algorithm with the un-cracked solution $\alpha = 0$. **b** Numerical results obtained using $\bar{\ell}$-refinement. *Each row* corresponds to a set of computations, each taking the one at its *left* as a first guess for u and α

In the case of a quasi-static evolution, Lancioni and Royer-Carfagni (2009) and Pham et al. (2011a) suggested that the internal length can be identified from the critical load at the onset of crack nucleation. In our context, where we only consider a *static* problem and focus on the limiting energy (4), this interpretation is not meaningful. Also, in the experiments, the initial state corresponds to that of the plug with many

existing disordered cracks and the mechanism leading to the selection of the steady state fracture pattern is the self-organization of those cracks and not that of loss of stability of the elastic solution. Hence, we stand by the interpretation that the regularization length is an artificial numerical parameter.

6.1.2 ℓ-refinement

To obtain an accurate resolution for complex crack patterns and, at the same time, avoid the persistence of the purely elastic solution, we implemented an $\bar{\ell}$-*refinement* technique. For a given loading $\bar{\epsilon}$ and mesh size h, we minimize the total energy $\mathcal{E}^{(\bar{\ell})}$ for decreasing values of the regularization length, initializing each computation with the α field obtained at the previous one. Figure 3b represents the outcome of such a series of computations highlighting, how this approach significantly reduces the sensitivity of the numerical results on the regularization length $\bar{\ell}$ and allows us to retrieve an accurate representation of a large family of crack geometries for small and high loadings. The outcome of this set of simulations may still depend on the initial value of $\bar{\ell}$. This value, 0.2 for Fig. 3b, is chosen large enough to avoid the persistence of the purely elastic solution and small enough to allow for localization of α within the domain. In practice, these two criteria do not give a large range for the choice of this parameter. The key properties of the final result of Figs. 3b and of the following Fig. 4b do not sensibly depend on the initial value of $\bar{\ell}$, provided that it fits within the (quite strict) criteria above.

Table 1 provides a quantitative comparison of the energies of the solutions of Fig. 3a, b for $\bar{\ell} = 0.05$. In each case, the configurations obtained using $\bar{\ell}$-refinement (last column of Fig. 3b) have a lesser energy than the one obtained through a direct computation (Fig. 3a). To obtain accurate values of the fracture energies with this choice of $h = \mathcal{O}(\bar{\ell})$, and following the discussion in Bourdin et al. (2008) (Sec 8.1.1 p.103), the reported surface energies are computed using the effective fracture toughness $G_c^{(num)} = G_c/(1 + 3h/8\bar{\ell})$.

6.1.3 Lowest energy crack shapes

For each drying intensity $\bar{\epsilon}$ we select the final cross-sectional crack geometry on the basis of a least energy criterion inspired by the global minimality

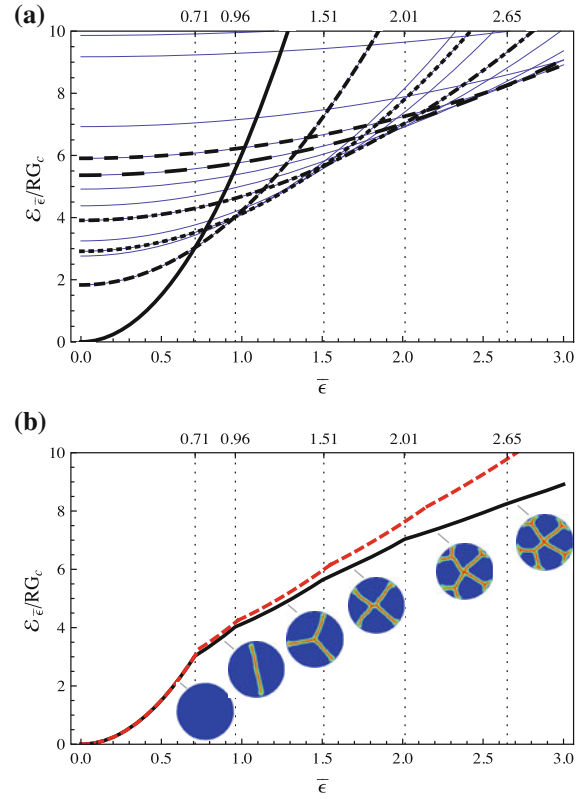

Fig. 4 Minimization over star-shaped cracks vs. minimization of functional (11). As the loading increases, our numerical method identifies crack configurations with much lower energetically than star-shaped cracks. **a** Energies associated with the crack geometries identified in Fig. 3b as a function of the loading parameter. *Thick black lines* distinguishes among all the *energy curves* (*blue lines*), the ones corresponding to configurations attaining the minimal energy for some value of the loading parameters. The *vertical dotted lines* correspond to the critical loading upon which the energy branch for which energy minimality is attained changes. Note that for large $\bar{\epsilon}$ the identification of critical loadings becomes difficult. **b** Comparison of the optimal energy obtained using minimization over star-shaped cracks (*dashed line*) and numerical simulation (*continuous line*). The *continuous line* is the *lower* envelope of the *curves* in Fig. 4a . The pictures represent the optimal crack shapes in each range of the loading parameter delimited by the *vertical dotted lines*

principle (12). To this end, we use a method similar to that in Sect. 4. Noticing that for a given α-field (i.e. crack geometry) the elastic part of the total energy (11) scales quadratically with the loading, one can calculate the total energy that each of the crack patterns obtained numerically for a given loading $\bar{\epsilon}^*$ would have for any $\bar{\epsilon}$. Figure 4a represents the total energy obtained in this way for each of the crack patterns in the last column of Fig. 3b. From this figure, for each $\bar{\epsilon}$, is possible to select the crack pattern with the lowest energy level.

Table 1 Energies of the numerical solutions in Fig. 3 for $\bar{\ell} = 0.05$ without (top) or with (bottom) $\bar{\ell}$-refinement

$\bar{\epsilon}$	Elastic	Surface	Total
0.6	2.2	0	2.2
0.8	3.9	0	3.9
1.0	6.0	0	6.0
1.2	8.7	0	8.7
1.4	1.6	3.9	5.5
1.6	2.0	4.0	6.0
1.8	1.9	4.9	6.8
2.0	2.0	5.3	7.3
2.2	2.1	5.7	7.8
2.5	2.1	6.4	8.5
3.0	2.1	7.3	9.4
4.5	2.3	9.6	11.8
5.0	2.4	9.8	12.2
$\bar{\epsilon}$	Elastic	Surface	Total
0.6	2.2	0	2.2
0.8	1.5	1.8	3.4
1.0	1.3	2.8	4.1
1.2	1.7	2.9	4.6
1.4	2.0	3.3	5.3
1.6	2.0	3.9	5.9
1.8	2.0	4.4	6.4
2.0	2.0	4.9	6.9
2.2	2.0	5.4	7.4
2.5	2.1	5.9	8.0
3.0	2.1	6.9	9.1
4.5	2.3	9.2	11.5
5.0	2.4	9.9	12.3

Amongst all the curves, the ones attaining the lowest energy for some value of the loading parameter are plotted in black and thicker line width. Their lower envelope is the continuous black line reported in Fig. 4b, together with the associated optimal crack geometries. Although it is of course never possible to prove global optimality, the crack geometries depicted in Fig. 4b are the lowest energy configurations we were able to attain, and the ones which we will compare with star-shaped cracks and experiments in the sequel.

6.2 Comparison with star-shaped cracks

Figure 4b compares the total energy of these configurations with the energy of the star-shaped cracks taken from Fig. 2 (dashed line). For small values of the loading parameter, we obtain similar geometries and critical loading. The surface energy obtained is close to the number of branches, and the critical loading upon which we obtain a single straight crack is 0.71 (vs. a theoretical value of $\bar{\epsilon}_2 = 0.73$). Bifurcation between straight and Y-shaped cracks take place at $\bar{\epsilon} \simeq 0.94$ (vs. a theoretical value of $\bar{\epsilon}_2 = 0.97$). More interestingly, for larger values of $\bar{\ell}$, our numerical simulations have identified multiple configurations that are energetically close to each other but always less expensive than star-shaped cracks. In particular, we show that perfect 5-branch stars are never optimal and that configurations consisting of either two triple junctions very close to each others (see for instance $\bar{\epsilon} = 1.6$ in Fig. 3b), a 4-branch star whose branches split in two near the tube boundary (see for instance $\bar{\epsilon} = 1.8, 2.0, 2.2$ in Fig. 3b), or a more complicated patterns like the "stick figure" looking 5 cracks configuration that we obtain for $\bar{\epsilon} = 2.5$ have lesser energy. Of course, that the local geometry near the crack crossing resembles 2 triple junctions near each others rather that an "X" does not really come up as a surprise. As mentioned earlier, the fracture energy (4) resembles the Mumford-Shah energy for edge segmentation (Mumford and Shah 1989). Therefore, it seems natural to expect that if they posses some form of regularity, optimal crack geometries satisfy the Mumford-Shah conjecture which rules out crack crossing, kinks and only allows cracks to meet at 120° triple junctions, locally.

6.3 Square tubes

Finally, we performed another set of numerical simulations on unit square tubes. The results obtained by the same $\bar{\ell}$-refinement method, as in Fig. 3b for circular tubes, are depicted on Fig. 5. The materials parameters and mesh size are unchanged ($E = 1$, $G_c = 1$, $\nu = 1$, $h = 0.025$). Whereas for circular tubes, star-shaped cracks are natural candidates, there were no obvious family of cracks in this case. This geometry also leads to a rich variety of crack patterns and highlights the strength of the proposed method in identifying complex crack patterns without *a priori* hypothesis. Some of the quantitative properties of the optimal cracks highlighted in the case of circular tubes are still observed. Again, cracks seem to split near the

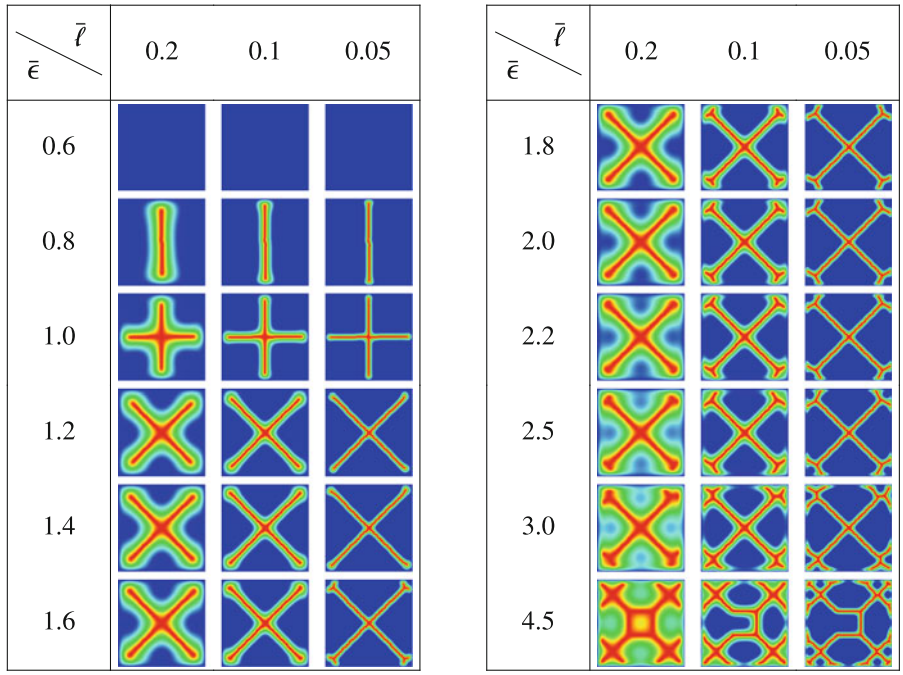

Fig. 5 Numerical results for *square tubes* by minimization of functional (11) using the $\bar{\ell}$-continuation method

edges of the tubes. Again, triple junctions seem to be favored over crack crossing, although in the case of two diagonal or longitudinal cracks, the resolution of our numerical experiments does not allow us to clearly identify the configuration. As for the circular tube, one can further post process the numerical result in order to identify the range of loadings for which each of the identified configuration is optimal. This is presented in Fig. 6. Again, for small values of the loading parameters, simple and somewhat predictable crack geometries are obtained. For larger values of $\bar{\epsilon}$, more complex and less intuitive patterns are energetically more advantageous.

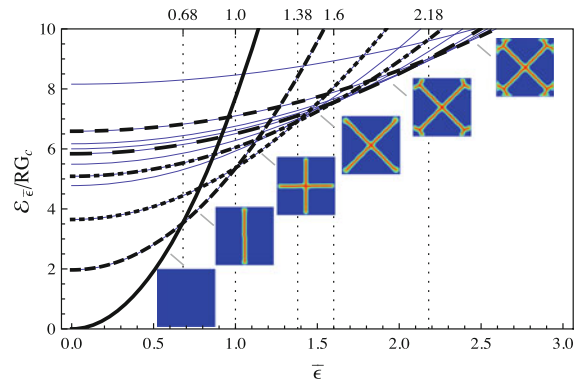

Fig. 6 Range of parameters in which the configuration identified in Fig. 5 are optimal. The *blue lines* correspond to the energy associated with cracks patterns that were identified in Fig. 5 but are never optimal

7 Comparison between experimental and numerical results

7.1 Identification of the loading parameter $\bar{\epsilon}$

Dimensional analysis shows that the model relies on a single parameter, $\bar{\epsilon}$ whose value needs to be estimated in order to perform quantitative comparison between experiments and numerical simulation. As $\bar{\epsilon}$ depends on experimental conditions, colloidal suspension type, and tube geometry, one solution is to try to measure separately ϵ_0, E, and G_c appearing in the definition (2) of $\bar{\epsilon}$. One may obtain the material constants E, G_c by indentation (Malzbender et al. 2002) and the mismatch strain ϵ_0 by beam deflection technics (Tirumkudulu and Russel 2004; Chekchaki et al. 2011) from a thin film drying experiments, for instance. However, such direct measurements are difficult, and transposing the values obtained from one type of experiments (thin film drying) to another (directional drying) is questionable. Indeed, the parameters may depend on the type of

Table 2 Values of Griffith's length L_c (in μm) for several Ludox®suspensions and drying rates (SV = [$T \simeq 3\,°C$ and RH $\leq 10\,\%$ or at $T \simeq 20\,°C$ and RH $\geq 90\,\%$] and HV = [$T \simeq 20\,°C$ and RH $\leq 10\,\%$])

L_c	Ludox®SM30 ($r \simeq 3.5$ nm)	Ludox®HS40 ($r \simeq 6$ nm)
HV	34 ± 10	40 ± 10
SV	60 ± 18	45 ± 15

experiments and even evolve in time. For example, the material constants E and G_c of the porous medium may depend on the microstructure, influenced by formation dynamics.

Instead of performing such difficult measurements, whose relevance to our problem may be questionable, we used the method presented in Gauthier et al. (2010), which we briefly summarize. The basis of the method is to consider a directional drying experiment in thin rectangular tubes (Allain and Limat 1995). In this geometry, an array of parallel tunneling cracks is obtained and the cracks spacing λ can be correlated with the Griffith length $L_c := EG_c/\sigma_0^2$ (σ_0 being the prestress induced by the film's drying). Using an energy minimization principle similar to the one in Sect. 4, one can show that the spacing λ is proportional to $\sqrt{L_c t}$, t being the tube's thickness and in particular, for $\nu = 0.3$, one obtains $\lambda \sim 3.1\sqrt{L_c t}$. For a given material and drying parameter, the value of L_c can therefore be deduced from measurements of λ. Table 2 presents the value of L_c for Ludox®SM30 ($r \simeq 3.5$ nm) and Ludox®HS40 ($r \simeq 6$ nm) under high velocity and slow velocity conditions.

We assume that the Griffith length L_c is a well-defined parameter for a given suspension and drying condition, and that it is independent of the cross-sectional geometry of the directional drying experiment. Hence, from the values of L_c in Table 2, we estimate the value of $\bar{\epsilon}$ in the directional drying of circular and square tubes of different diameters using the relation (7), which gives $\bar{\epsilon} = 0.52\sqrt{R/L_c}$ for $\nu = 0.3$.

7.2 Results and analysis

Table 3 reports on the series of experiments on circular tubes described in Sect. 2. From a *qualitative* standpoint we observe that star-shaped appear above a critical load, and that the number of branches increases with the loading, which is consistent with the analysis in Sect. 4 and the numerical simulations of Sect. 6. In order to perform a *quantitative* comparison, we summarize all the results obtained in the case of circular tubes in Fig. 7. The first row corresponds to the outcome of the semi-analytical minimization over star-shaped cracks: the critical values of the loading parameters computed in Sect. 4 upon which bifurcation between different morphologies take place is printed in red letters, and represented by red dashed vertical lines. The second row corresponds to the numerical experiments without *a priori* hypotheses on the crack path. The critical loads extracted from Fig. 4a are printed in black letters, and represented by vertical solid black lines. As highlighted in Fig. 4b, the critical loads obtained in the case of the bifurcation from γ_1 to γ_2, then γ_3 and γ_4 are very close. This part of the table can be seen as a *verification* of the numerical implementation, i.e. as evidences that the computed solutions are indeed solution of the variational fracture model. The third row summarizes the outcome of the experiments from Table 3. For each experiment, the value of the loading parameter is shown together with the accuracy of the measurement. When available, pictures of the cross sections are also displayed. We observe that for every single choice of $\bar{\epsilon}$, the crack geometry predicted by our approach matches the one observed in the experiment. This acts as a *validation* of the variational fracture model as a predictive tool in the setting of drying of colloidal suspension.

We also did a single experiment on a square tube, for an estimated value $\bar{\epsilon} \simeq 1.8$ of the loading parameter for which we obtained two diagonal cracks (see the bottom image in Figure 1b). Again, the numerical simulation in this case matches the experiment (see Figs. 5 and 6).

Despite the modeling simplifying assumption, the complexity of the numerical technique, and the uncertainty of the measurement of the parameters, the agreement between analysis, simulation, and experiments is excellent. Our model correctly captures the essential physics of the crack formation giving credit to the idea that crack growth can be predicted by minimization of the sum of elastic and surface energy over all possible crack path. In order to further justify this idea, one will need to compare experiments and simulations for higher loading parameters $\bar{\epsilon}$ in which case numerical simulations identify complex crack patterns with significantly lower energy than classical star-shaped solutions. For instance, better quality imaging will be required to unambiguously determine if the 5 cracks

Table 3 Experimental results on circular tubes. The value of n corresponds to the number of sectors delimited by the cracks as in Sect. 4

	Ludox®	HV/SV	L_c (μm)	R (μm)	n	$\bar{\epsilon}$
a	SM30	HV	34 ±10	50 ± 5	1	0.6 ± 0.12
b	SM30	SV	60 ±18	150 ± 15	2	0.8 ± 0.16
c	SM30	SV	60 ±18	500 ± 50	3	1.5 ± 0.30
d	HS40	SV	45 ±15	500 ± 50	4	1.7 ± 0.37
e	HS40	HV	40 ±10	500 ± 50	4	1.8 ± 0.27
f	SM30	HV	34 ±10	500 ± 50	4	2.0 ± 0.39
g	HS40	HV	40 ±10	750 ± 75	5	2.3 ± 0.41
h	SM30	HV	34 ±10	750 ± 75	5	2.4 ± 0.48

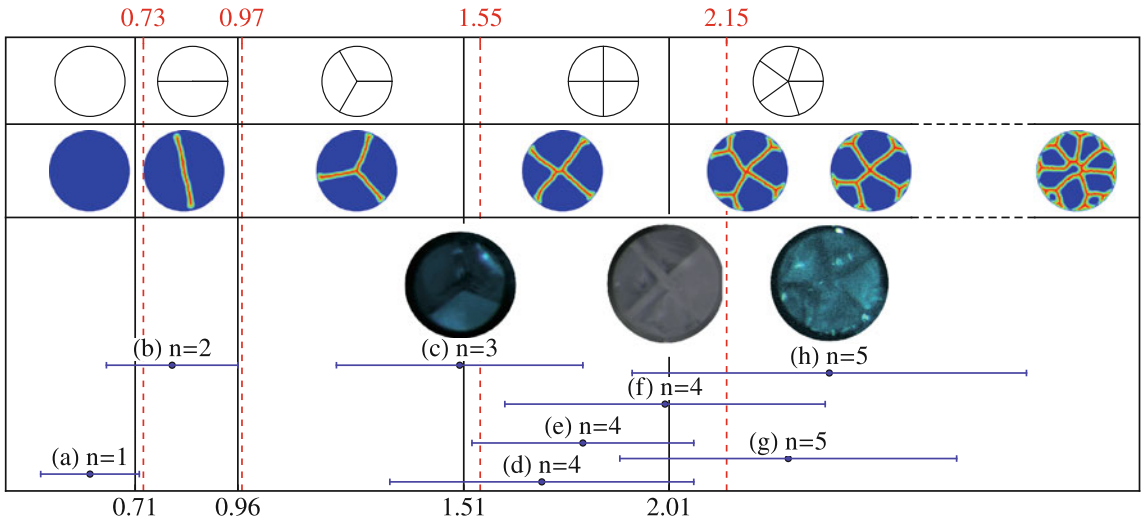

Fig. 7 Comparison between semi-analytical, numerical and experimental results for circular tubes

configurations we observe experimentally (see Fig. 1b or 7) resembles a "stick figure" as in our numerical simulation (cf. Fig. 3 for $\bar{\epsilon} = 2.5$), a regular 5-branch star, or something completely different.

8 Conclusions and future work

In this paper, we have shown that a numerical implementation (Bourdin et al. 2000) of the variational approach to fracture mechanics (Francfort and Marigo 1998) enhanced with a selection criterion is capable to qualitatively and quantitatively predict complex crack shapes starting from an undamaged material. For this, we have studied some unidirectional drying experiments of colloidal suspensions performed in capillary tubes where solvent evaporation leads to the formation of a growing porous solid medium. In these experiments, adhesion on the tubes walls combined with shrinkage lead to high tensile stresses and give rise to cracks whose morphologies depend on the tube geometry and the drying velocities. We verified that the changes in crack geometry can be accounted by a two-dimensional static simple model depending on a single dimensionless parameter $\bar{\epsilon}$ which represents the ratio of the bulk elastic energy (which depends on the intensity of the tensile strain induced by drying) over the cost of fracture. Under the assumption that cracks are star-shaped, the number of branches has been obtained as a function of the loading parameter.

We then presented a numerical method based on the regularization of the total energy introduced in the variational model, and enhanced it with a selection principle and a refinement method. For small enough values of the loading, this allowed us to verify that star-shaped cracks are actually favored in circular tubes, to predict cracks shapes in square tubes and to achieve qualitative and quantitative agreement between numerical simulation, semi-analytical solutions and experiments. This results are summarized in Fig. 7. For higher values of the loading parameters, more complex cracks geometries are observed. These are the situations where the virtue of the variational approach to fracture over more conventional ones requiring at least some *a priori* knowledge of the crack path becomes more striking. But at this point, though, we were not able to compare them with experiments that will require additional work in order to deal with larger tubes for instance. In these situations, the main difficulty is the *post-mortem* analysis of the crack geometry. Microphotography though the sides of the tubes becomes hard to interpret, and cutting the tubes without perturbing the cracks geometry is difficult. Perhaps the solution lies in full three-dimensional imaging of the tubes and post-processing in order to highlight the location of the cracks.

From the modeling perspective, a full three-dimensional linear poroelasticity model (Biot 1941) would be welcome in particular to study the entire propagation from the crack initiation to the crack self-organisation. The complexity of this task mainly lies in the time-dependence of the solid domain and of the material constants. Finally, from a physico-chemical point of view, the link between the drying velocity and the macroscopic $\bar{\epsilon}$ signature will have to be explored.

Acknowledgments The work of VL and GG was partially supported by the ANR Program JC-JC ANR-05-JCJC-0029 Morphologies. CM gratefully acknowledges the funding of the French National Research Council (CNRS) for a PICS bilateral exchange program with BB and a grant of the University Pierre et Marie Curie EMERGENCES-UPMC. BB's work was supported in part by the National Science Foundation under the grant DMS-0909267. Some of the numerical experiments were performed using resources of the Extreme Science and Engineering Discovery Environment (XSEDE), which is supported by National Science Foundation grant number OCI-1053575, provided by TACC at the University of Texas under the Resource Allocation TG-DMS060014N and the resources of the Institut du Développement et des Ressources en Informatique Scientifique (IDRIS) under the DARI 2011 allocation 100064.

References

Adda-Bedia M, Pomeau Y (1995) Crack instabilities of a heated glass strip. Phys Rev E 52(4, Part b):4105–4113

Allain C, Limat L (1995) Regular patterns of cracks formed by directional drying of a colloidal suspension. Phys Rev Lett 74:2981–2984

Ambrosio L, Fusco N, Pallara D (2000) Functions of bounded variation and free discontinuity problems. Oxford Mathematical Monographs, Oxford Science Publications

Ambrosio L, Tortorelli V (1990) Approximation of functionals depending on jumps by elliptic functionals via Γ-convergence. Commun Pure Appl Math 43(8):999–1036

Ambrosio L, Tortorelli V (1992) On the approximation of free discontinuity problems. Boll Un Mat Ital B (7) 6(1):105–123

Amor H, Marigo J-J, Maurini C (2009) Regularized formulation of the variational brittle fracture with unilateral contact: Numerical experiments. J Mech Phys Solids 57(8): 1209–1229

Bahr H-A, Hofmann M, Weiss H-J, Bahr U, Fischer G, Balke H (2009) Diameter of basalt columns derived from fracture mechanics bifurcation analysis. Phys Rev E (Stat Nonlinear Soft Matter Phys) 79(5):056103

Bahr H, Weiss H, Bahr U, Hofmann M, Fischer G, Lampenscherf S, Balke H (2010) Scaling behavior of thermal shock crack patterns and tunneling cracks driven by cooling or drying. J Mech Phys Solids 58(9):1411–1421

Balay S, Brown J, Buschelman K, Eijkhout V, Gropp W, Kaushik D, Knepley M, Curfman McInnes L, Smith B, Zhang H (2010) PETSc users manual. Technical report ANL-95/11, revision 3.1, Argonne National Laboratory

Balay S, Brown J, Buschelman K, Gropp W, Kaushik D, Knepley M, McInnes LC, Smith B, Zhang H (2011) PETSc Web page. URL:http://www.mcs.anl.gov/petsc

Balay S, Gropp W, Curfman McInnes L, Smith B (1997) Efficient management of parallelism in object oriented numerical software libraries. In: Arge E, Bruaset AM, Langtangen HP (eds) Modern software tools in scientific computing. Birkhäuser Press, London, pp 163–202

Bažant Z (1999) Size effect on structural strength: a review. Arch Appl Mech 69:703–725

Bažant Z, Ohtsubo H, Aoh K (1979) Stability and post-critical growth of a system of cooling or shrinkage cracks. Int J Fract 15(5):443–456

Bellettini G, Coscia A (1994) Discrete approximation of a free discontinuity problem. Numer Funct Anal Optim 15(3–4): 201–224

Benson S, Curfman McInnes L, Moré J, Munson T, Sarich J (2010) TAO user manual (revision 1.10.1). Technical report ANL/MCS-TM-242, Mathematics and Computer Science Division, Argonne National Laboratory. URL:http://www.mcs.anl.gov/tao

Biot MA (1941) General theory of 3-dimensional consolidation. J Appl Phys 12:155–164

Bourdin B (1999) Image segmentation with a finite element method. M2AN Math Model Numer Anal 33(2):229–244

Bourdin B (2007) Numerical implementation of the variational formulation of quasi-static brittle fracture. Interfaces Free Bound 9:411–430

Bourdin B, Francfort GA, Marigo JJ (2000) Numerical experiments in revisited brittle fracture. J Mech Phys Solids 48(4):797–826

Bourdin B, Francfort GA, Marigo J-J (2008) The variational approach to fracture. J Elast 91(1):5–148

Braides A (1998) Approximation of free-discontinuity problems, vol. 1694 of Lecture Notes in Mathematics, Springer

Braides A (2002) Γ-convergence for beginners, Vol. 22 of Oxford Lecture Series in mathematics and its applications. Oxford University Press, Oxford

Branagan D, Cairns H (1993) Tessalated pavements in the Sydney region, New South Wales. J Proc Roy Soc New South Wales 126(1):63–72

Burke S, Ortner C, Süli E (2010) An adaptive finite element approximation of a variational model of brittle fracture. SIAM J Numer Anal 48(3):980–1012

Chambolle A (1999) Finite-differences discretizations of the Mumford-Shah functional. M2AN Math Model Numer Anal 33(2):261288

Chekchaki M, Frelat J, Lazarus V (2011) Analytical and 3D finite element study of the deflection of an elastic cantilever bilayer plate. J Appl Mech T ASME 78(1):011008

Colina H, Roux S (2000) Experimental model of cracking induced by drying shrinkage. Eur Phys J E 1(2–3):189–194

Corson F, Adda-Bedia M, Henry H, Katzav E (2009) Thermal fracture as a framework for quasi-static crack propagation. Int J Fract 158(1):1–14

Dal Maso G (1993) An introduction to Γ-convergence. Birkhäuser, Boston

DeGraff J, Aydin A (1987) Surface morphology of columnar joints and its significance to mechanics and direction of joint growth. Geol Soc Am Bull 99:600–617

Del Piero G, Lancioni G, March R (2007) A variational model for fracture mechanics: numerical experiments. J Mech Phys Solids 55(12):2513–2537

Dufresne E, Corwin E, Greenblatt N, Ashmore J, Wang D, Dinsmore A, Cheng J, Xie X, Hutchinson J, Weitz D (2003) Flow and fracture in drying nanoparticle suspensions. Phys Rev Lett 91(22):224501

Dufresne E, Stark D, Greenblatt N, Cheng J, Hutchinson J, Mahadevan L, Weitz D (2006) Dynamics of fracture in drying suspensions. Langmuir 22(17):7144–7147

Francfort GA, Marigo J-J (1998) Revisiting brittle fracture as an energy minimization problem. J Mech Phys Solids 46: 1319–1342

Freddi F, Royer-Carfagni G (2010) Regularized variational theories of fracture: a unified approach. J Mech Phys Solids 58(8):1154–1174

Gauthier G, Lazarus V, Pauchard L (2007) Alternating crack propagation during directional drying. Langmuir 23(9): 4715–4718

Gauthier G, Lazarus V, Pauchard L (2010) Shrinkage star-shaped cracks: explaining the transition from 90 degrees to 120 degrees. EPL 89:26002

Goehring L, Morris SW, Lin Z (2006) Experimental investigation of the scaling of columnar joints. Phys Rev E (Stat Nonlinear Soft Matter Phys) 74(3):036115

Griffith A (1920) The phenomena of rupture and flow in solids. Philos Trans R Soc Lond 221:163–198

Hakim V, Karma A (2009) Laws of crack motion and phase-field models of fracture. J Mech Phys Solids 57(2):342–368

Hofmann M, Bahr H, Linse T, Bahr U, Balke H, Weiss H (2006) Self-driven tunneling crack arrays—a 3D-fracture mechanics bifurcation analysis. Int J Fract 141(3–4):345–356

Jenkins D (2009) Determination of crack spacing and penetration due to shrinkage of a solidifying layer. Int J Solids Struct 46(5):1078–1084

Lancioni G, Royer-Carfagni G (2009) The variational approach to fracture mechanics: a practical application to the french Panthéon in Paris. J. Elast 95(1–2):1–30

Lazarus V, Pauchard L (2011) From craquelures to spiral crack patterns: influence of layer thickness on the crack patterns induced by desiccation. Soft Matter 7(6):2552–2559

Malzbender J, den Toonder JMJ, Balkenende AR, de With G (2002) Measuring mechanical properties of coatings: a methodology applied to nano-particle-filled sol-gel coatings on glass. Mater Sci Eng R 36(2–3):47–103

Mangold N (2005) High latitude patterned grounds on mars: classification, distribution and climatic control. Icarus 174(2): 336–359

Muller G (1998) Starch columns: analog model for basalt columns. J Geophys Res 103(B7):15239–15253

Mumford D, Shah J (1989) Optimal approximations by piecewise smooth functions and associated variational problems. Commun Pure Appl Math 42:577–685

Nemat-Nasser S, Sumi Y, Keer L (1980) Unstable growth of tension cracks in brittle solids - stable and unstable bifurcations, snap-through, and imperfection sensitivity. Int J Solids Struct 16(11):1017–1035

Negri N (1999) The anisotropy introduced by the mesh in the finite element approximation of the Mumford-Shah functional. Numer Funct Anal Optim 20(9–10):957–982

Pham K, Amor H, Marigo J-J, Maurini C (2011a) Gradient damage models and their use to approximate brittle fracture. Int J Damage Mech 20(4):618–652

Pham K, Marigo J-J, Maurini C (2011b) The issues of the uniqueness and the stability of the homogeneous response in uniaxial tests with gradient damage models. J Mech Phys Solids 59(6):1163–1190

Plug L, Werner B (2001) Fracture networks in frozen ground. J Geophys Res Earth 106(B5):8599–8613

Ronsin O, Heslot F, Perrin B (1995) Experimental study of quasistatic brittle crack propagation. Phys Rev Lett 75(12): 2352–2355

Saliba R, Jagla EA (2003) Analysis of columnar joint patterns from three-dimensional stress modeling. J Geophys Res Solid Earth 108(B10):2476

Seilacher A (2001) Concretion morphologies reflecting diagenetic and epigenetic pathways. Sediment Geol 143(1–2): 41–57

Shinn E (2009) The mystique of beachrock. Special publication of the International Association of Sedimentologists 41(1):19–28

Tirumkudulu M, Russel W (2004) Role of capillary stresses in film formation. Langmuir 20(7):2947–2961

Toramaru A, Matsumoto T (2004) Columnar joint morphology and cooling rate: a starch-water mixture experiment. J Geophys Res 109(B2):B02205

Yang B, Ravi-Chandar K (2001) Crack path instabilities in a quenched glass plate. J Mech Phys Solids 49(1):91–130

Yuse A, Sano M (1993) Transition between crack patterns in quenched glass plates. Nature 362(6418):329–331